Available online at www.sciencedirect.com
ScienceDirect
Journal of the European Ceramic Society 30 (2010) 2223–2237
www.elsevier.com/locate/jeurceramsoc

Atomistic analyses of the effect of temperature and morphology on mechanical strength of Si–C–N and Si–C–O nanocomposites

Vikas Tomar*, Ming Gan, Han Sung Kim

School of Aeronautics and Astronautics, Purdue University, 701 West Stadium Ave, West Lafayette, IN 47906, USA

Available online 28 March 2010

Abstract

3-D molecular dynamics (MD) analyses of SiC–Si_3N_4 nanocomposite deformation and SiCO nanocomposite deformation are performed at 300 K, 900 K, and 1500 K. In SiC–Si_3N_4 nanocomposites, distribution of second phase SiC particles, volume fraction of atoms in GBs, and GB thickness play an important role in temperature dependent mechanical behavior. The deformation mechanism is a trade-off between the stress concentration caused by SiC particles and Si_3N_4–Si_3N_4 GB sliding. The temperature increase tends to work in favor of GB sliding leading to softening of structures. However, microstructural strength increases with increase in temperature when GBs are absent. In the case of SiCO nanocomposites, findings indicate that temperature change dependent amorphization of nanodomains, the nanodomain wall placement, the nanodomain wall thickness, and nanodomain size are important factors that directly affect the extent of crystallinity and the strength against mechanical deformation.

Keywords: Nanocomposites; Failure analysis; Si_3N_4; SiC; SiO_2

1. Introduction

Silicon carbide (SiC)–silicon nitride (Si_3N_4) nanocomposites and silicon oxide-carbide (SiCO) nanocomposites are two future important high temperature materials. SiC–Si_3N_4 nanocomposites with nano-sized SiC particles placed either in micro-sized Si_3N_4 grains or along Si_3N_4 grain boundaries (GBs) have been shown to be exceptionally strong at a range of temperatures.[1–5] Factors that affect the strength of the SiC–Si_3N_4 nanocomposites can include the second phase SiC particle placement and clustering along Si_3N_4 GBs, the SiC particle size, Si_3N_4 grain size, and Si_3N_4 matrix morphology. Similarly SiCO nanocomposites have been shown to be promising for high temperature applications.[6–8] Two different morphological forms of SiCO nanocomposites have been proposed in the literature: (1) morphologies in which SiO_2 nanodomains are separated by graphitic carbon nanodomain boundaries,[8–10] and (2) morphologies in which SiC and SiO_2 nanodomains are mixed together.[7] Factors that could affect the temperature dependent mechanical strength of such nanocomposites include nanodomains size, thickness of nanodomain boundaries, size of SiC and SiO_2 nanodomains, etc. With such varied factors affecting temperature dependent mechanical strength, an understanding of how such factors individually influence the nanocomposite properties is required. Such understanding can be extrapolated to fundamental developments on combined effects of such factors on the nanocomposite mechanical strength using analytical relations. Since most microstructural features are at the nanoscale, an individual understanding of property influencing factors requires atomistic analyses.

Recently, the effect of morphological variations resulting from second phase SiC particle placement and changes in GB strength on the room temperature fracture strength of SiC–Si_3N_4 nanocomposites was analyzed using a mesoscale cohesive finite element method (CFEM) and using molecular dynamics (MD) based analyses.[11–14] The analyses have revealed that high strength and relatively small sized SiC particles act as stress concentration sites in Si_3N_4 matrix leading to inter-granular Si_3N_4 matrix cracking as a dominant nanocomposite failure mode under dynamic loading. At high SiC volume fractions that peak at approximately 30%, the CFEM analyses have revealed that due to a significant number of nano-sized SiC particles being present in micro-sized Si_3N_4 matrix, the SiC particles invariantly fall in the wake regions of microcracks leading to significant increase in fracture resistance. This finding was mechanistically confirmed in the room temperature MD analyses that revealed that particle clustering along the GBs was more effective than particles being placed on GBs in increasing the nanocompos-

* Corresponding author. Tel.: +1 765 494 3423; fax: +1 765 494 0307.
E-mail address: tomar@purdue.edu (V. Tomar).

0955-2219/$ – see front matter © 2010 Elsevier Ltd. All rights reserved.
doi:10.1016/j.jeurceramsoc.2010.03.002

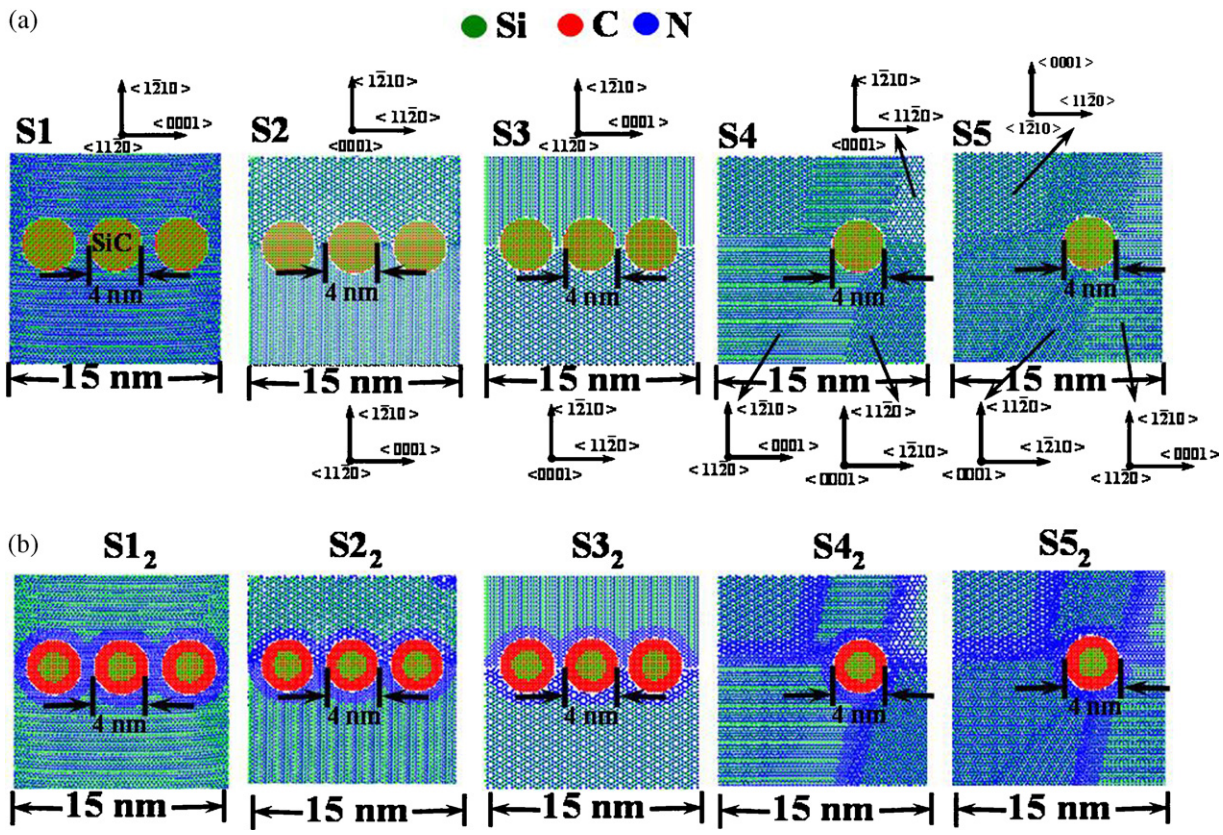

Fig. 1. Set of Si–C–N atomistic microstructures analyzed.

ite mechanical strength. Since both CFEM and MD analyses were performed at room temperature, the role of temperature in changing the explained mechanisms remains to be analyzed.

The SiC–Si_3N_4 nanocomposite analyses have so far assumed the presence of sharp interfaces and GBs (interfaces at which transition from one phase to another is immediate with zero interface width and GBs where such transition is immediate with zero GB width). In reality, while some SiC–Si_3N_4 nanocomposite morphologies have sharply defined interfaces, e.g. TEM image shown in Fig. 10 on SiC–Si_3N_4 interfaces by Ref. 15, other SiC–Si_3N_4 nanocomposite morphologies have diffusion of C, N, or Si atoms at the interfaces and GBs resulting in both having a finite width.[16] In the present work, classical MD based nanoscale mechanical strength analyses at 300 K, 900 K, and 1500 K are performed to analyze the effect of SiC particle placement with respect to Si_3N_4 GBs and the effect of change in Si_3N_4 GB and SiC–Si_3N_4 interface thicknesses on temperature dependent mechanical strength of SiC–Si_3N_4 nanocomposites. Similar analyses in the case of Si–C–O nanocomposites focus on the effect of nanodomain size, the effect of changes in domain boundary thickness, and the effect of change in SiCO morphology type on the resulting temperature dependent mechanical strength.

Classical MD replaces a comprehensive quantum mechanical treatment of interatomic forces with a phenomenological description in the form of an interatomic potential. Classical MD based atomistic analyses of the nanocomposite mechanical deformation as a function of phase morphology are relatively new and have focused on a very limited sets of issues in metallic, polymer–clay, and ceramic nanocomposites.[17–21] Both SiC and Si_3N_4 have been individually analyzed in the atomistic simulations for different mechanical strength related issues.[22–25] However, SiC–Si_3N_4 nanocomposite morphologies are analyzed in this work for the first time for understanding temperature dependent strength. This work is an extension of our earlier work on understanding the effect of SiC particle clustering and SiC particle size on the room temperature mechanical strength of the SiC–Si_3N_4 nanocomposites using classical MD.[13,14] In the case of SiCO nanocomposites, the present work is the first atomistic study of the nanomechanical deformation.

2. Formulation

In the case of SiC–Si_3N_4 nanocomposites, 3-D morphologies with cylindrical SiC particles distributed along different configurations of Si_3N_4 GBs are analyzed, Fig. 1. Computational limitations resulted in the maximum Si_3N_4 block size of 15 nm × 15 nm × 15 nm in all the microstructures. Analyses focus on the effect of placing SiC particles with respect to various GB configurations on the strength of the SiC–Si_3N_4 nanocomposites. Periodic boundary conditions (PBCs) are imposed in all three Cartesian directions. Such setting leads to the composite microstructure boxes shown in Fig. 1 repeating in x–y–z directions and representing a monolithic bulk composite.

Earlier, it has been reported[13,14] that particle size variation within few nanometers of diameter (2 nm vs. 4 nm) as well as

inter-particle spacing changes within few nm (1 nm vs. 3 nm) does not have significant effect on the SiC–Si_3N_4 nanocomposite mechanical strength. Based on these findings, owing to the computational limitations, structures with only one cylindrical SiC particle size with diameter equal to 4 nm are analyzed. Since previous calculations revealed that slight changes in inter-particle spacing do not affect deformation mechanism and strength, the analyses focused on keeping the SiC particles along GBs within 1 nm spacing. These morphologies are the same as used in the earlier reported analyses.[13,14] Analyses are performed on these morphologies to maintain continuity with the earlier reports. Doing so also introduces a very high volume fraction of SiC at the GBs along the loading direction. This should be taken as one limitation of the reported study. All SiC–Si_3N_4 interfaces in this study are concentrated in a small region. Such placement, therefore, also helped in understanding the role of SiC–Si_3N_4 interfaces in the nanocomposite mechanical deformation in a clearer way.

It is expected that higher inter-particle spacing should change the deformation mechanism as well as mechanical strength values. We cannot replicate experimental inter-particle spacing (>10 nm) owing to the limitations on the size of simulation structure while performing simulations using a realistic interatomic potential. Within this respect, the present simulations should be seen as an extreme case of being able to closely place second phase particles at precise locations on primary phase GBs. The resulting deformation mechanisms and mechanical strength values arising out of such simulations can be used as a guideline for developing constitutive relations for describing temperature and phase morphology dependent material behavior in such idealized settings. Such constitutive relations can be modified based on experimental considerations and morphologies for a wider applicability.

SiCO nanocomposites are generated based on the two different types of possible morphologies shown in literature: (1) morphology in which SiO_2 nanodomains are separated by graphitic carbon domain boundaries,[8–10] Fig. 2(a), and (2) morphology in which SiC and SiO_2 particles are mixed together,[7] Fig. 2(b). In the case of the first type of morphology (type-I), three different nanodomain sizes (9 nm, 6 nm and 4 nm) with two different domain wall thicknesses (0.5 nm $S6_1$, $S7_1$, $S8_1$ and 1 nm $S6_2$, $S7_2$, $S8_2$) consisting of graphitic carbon are considered. In the case of the second type of morphology (type-II), three different samples with three different mean domain sizes (9 nm, 6 nm and 4 nm) are considered. Orientation of grains in nanodomains is chosen randomly. In all instances, 15 nm × 15 nm × 15 nm block size of microstructures with PBCs imposed in all directions is analyzed. MD simulations are performed using a well established nanocomposite MD simulations framework.[19,26]

2.1. MD framework

The SiC–Si_3N_4 microstructures are formed by placing SiC cylindrical particles in Si_3N_4 blocks that have holes of sizes corresponding to the SiC particles. Setting up of the SiC–Si_3N_4 interface can critically affect the internal stresses in microstructures. In order to relieve any artificial internal stresses, first Si_3N_4 blocks with the holes were prepared and equilibrated without the presence of the corresponding SiC cylindrical particles. SiC particles were separately equilibrated as clusters. After equilibration, the Si_3N_4 block and the corresponding SiC particle were put together to form SiC–Si_3N_4 nanocomposites. Afterwards, the SiC–Si_3N_4 composite structures were again equilibrated. Such elaborate equilibration procedure was chosen so that the stress gradient at the SiC–Si_3N_4 interface in the nanocomposites was at the minimum. We observed a large stress gradient at the SiC–Si_3N_4 interface if the whole nanocomposite structure was equilibrated without separate equilibration of SiC inclusions and Si_3N_4 matrix phase. A gap of 2 Å was ensured between the SiC particles and the corresponding Si_3N_4 block's hole in order to prevent additional buildup of the internal stresses. However, changing the gap did not influence the observed trends and results. MD equilibration period was determined based on convergence in energy values. Within the MD equilibration time period we did not observe any phase transformation due to particle-matrix interactions. In the case of SiCO system, the microstructures of type-I were generated by placing graphitic carbon with two different thicknesses (5 Å and 10 Å) along the SiO_2 phase boundaries. MD equilibration resulted in the graphitic carbon as well as SiO_2 nanodomains changing phase type from being crystalline to being amorphous. For type-II morphology, nanocomposites of SiO_2 and SiC were generated with 50% volume fraction each. The MD equilibration resulted in SiO_2 acquiring amorphous structure while SiC continuing to be mainly crystalline.

2.1.1. Interatomic potential

Classical MD simulations of Si_3N_4 + SiC material systems require an interatomic potential to describe Si–Si, Si–N, Si–C, N–N, C–C, and N–C interactions. The potential should be fitted to the properties of Si_3N_4, SiC and to an approximation to the interfacial transitions between these components. Si_3N_4 family consists of two polymorphic members, α and β. The higher symmetry β phase has a hexagonal lattice (space groups $C^2{}_{6h}$, N176) with a primitive cell containing two Si_3N_4 formula units (a = 7.606 Å, c = 2.909 Å). The lower symmetry α phase is trigonal (space groups $C^4{}_{3v}$, N159) and has a primitive cell nearly twice as large (a = 7.746 Å, c = 5.619 Å) with twice as many atoms. The interatomic potentials for Si_3N_4 material system have been developed by Refs. 27–30. Of all these approaches, we choose the potential by Kroll[29] (based on Tersoff's potential) to model β-Si_3N_4 because of its simplicity and its ability to enable large scale MD simulations. β-Si_3N_4 is chosen because of its relative abundance in comparison to the α form. This potential has been shown to be thermally and structurally stable for various Si–N configurations by Ref. 31. Using this potential we studied temperature dependence of the elastic modulus of β-Si_3N_4. The results were in accordance with the available trend in the data from Ref. 32.

Different polytypes of SiC exist at ambient pressure, which are differentiated by the stacking sequence of the tetrahedrally bonded Si–C bilayers.[33] Among these polytypes, β-SiC (cubic-SiC) is of much interest for its electronic properties. In particular,

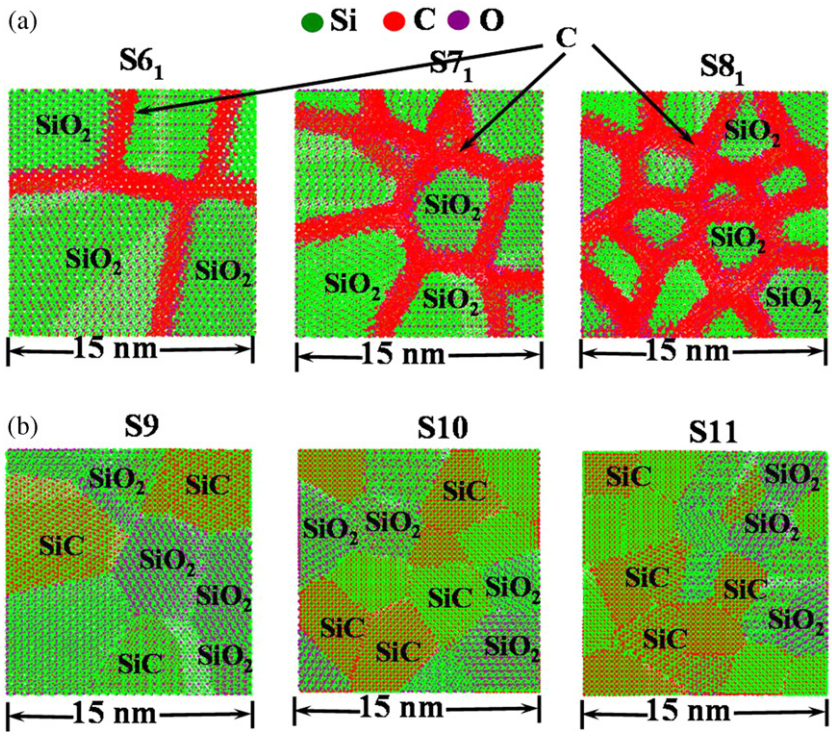

Fig. 2. Set of Si–C–O atomistic microstructures analyzed.

in recent years many theoretical and experimental studies have been carried out to investigate the different properties and possible applications of this material. Majority of interatomic potentials developed for SiC material system focus on describing the material properties of β-SiC.[34–37] We choose Tersoff's bond order potential to model interatomic interactions in SiC. For modeling SiO_2 system we chose another Tersoff potential form.[38] These are well known potential which have been shown to be applicable to describe temperature dependent mechanical properties of SiC and SiO_2, respectively. The melting point of Si_3N_4 is approximately 2700 K, of SiC is approximately 3100 K, and of SiO_2 is approximately 2000 K. The classical potentials usually perform very well until approximately 90% of the melting point temperatures. The simulation temperatures are approximately within 75% of these temperature values. At the interfaces of SiC and Si_3N_4 we need to be able to describe Si–C, Si–Si, C–N, and Si–N interactions. Tersoff's potential is useful only for describing the bulk Si–C, Si–Si, and Si–N interactions. We use potential developed for carbonitrides[39] to describe C–N interactions.

2.1.2. *High performance computing and mechanical deformation algorithm for MD simulations*

MD simulations are performed using a modified version of a scalable parallel code, DL_POLY 2.14.[40,41] The code has been modified and tested on a system of 1,000,000 atoms for a model ceramic matrix composite ($Al + Fe_2O_3$) material system and is benchmarked for scalable high performance classical MD simulations for large atomic ensembles with millions of atom. The simulations primarily focus on obtaining virial stress vs. strain relations and visual atomistic deformation information in order to delineate the deformation mechanisms. During stretching, the MD computational cell is stretched in the loading direction using a modified version of the NPT equations of motion of Ref. 42. NPT equations ensure that the structure has lateral pressure relaxed to atmospheric values during deformation. In this algorithm, the rate of change of a simulation cell volume, $V(t)$, is specified using a barostat friction coefficient parameter η such that

$$\frac{d\eta(t)}{dt} = \frac{1}{Nk_B T_{ext}\tau_P^2} V(t)(P - P_{ext}), \quad (1)$$

and

$$\frac{dV(t)}{dt} = 3\eta(t)V(t). \quad (2)$$

Here, P is the instantaneous pressure, P_{ext} is the externally applied pressure, N is total number of atoms in the system, k_B is the Boltzmann constant, T_{ext} is the external temperature, and τ_P is a specified time constant for pressure fluctuations. During the simulations, the system is initially equilibrated at $T_{ext} = 300$ K. After equilibration, the computational cell is stretched in the loading direction using $\eta = 0.01$ ps^{-1} for strain rate of 10^9 s^{-1}. This results in a tensile uniaxial stress loading in the x-direction, while the y- and z-directions have atmospheric stresses imposed upon the system.

In general, MD's time step limitations make it unsuitable to be used as a predictive technique for performing small strain rate mechanical deformation. High strain rate is a limitation of MD as a method and results of the MD simulations need to be interpreted while keeping this in mind. The values of $\gamma = 0.5$ and $P_{ext} = 1$ atmospheric pressure are used. The values for η and γ

are calculated in trial calculations that focused on achieving the best balance between simulation time (low η results in long simulation times and vice versa) and pressure fluctuations (high γ results in excessive pressure damping with increase in residual stresses along periodic boundaries). In the analyses reported in the manuscript, the MD equilibration time in between the periods of stretching is chosen as 2.0 ps. The equilibration time for 2 ps is chosen such that the total potential energy fluctuation of the system with respect to time is minimized. The change in time from 2 ps to longer did not change the simulation results. Keeping in mind the limitations of MD simulations in terms of time-steps we did not see any benefit in using the increased equilibration period.

3. Mechanical deformation results and analyses

Results of the MD simulations are analyzed by using visuals observations of defects, by plotting radial distribution functions (RDFs) and by plotting virial stress–true strain relations. Virial stress represents internal resistance offered by a material to an externally imposed load.[43] Since virial stress is an internal quantity, it is also an indicator of the increase in the stress concentration caused by the presence of an inhomogeneity in an otherwise homogenous body. With increase in inhomogeneity and ensuing stress concentration increase, material strength will reduce leading to a reduction in peak stress. It is important to note here that stress–strain based results from MD are at very high strain rates on very pure idealized samples. Due to high rates and high purity, strength value predictions are very high in MD simulations. In the absence of experiments at such high strain rates as used in MD, it is not possible to verify or deny MD simulation results. At small scales, experiments such as nanoindentation tests have also predicted very high strength of materials. However, the measurements in such experiments have been performed at very small scales under boundary constraints. The strain rates in such experiments are also much smaller than those in MD simulations. In the absence of experimental validations, MD simulation results can be used to predict trends on the effect of morphology on strength. Trends from MD simulations have been earlier verified in limited sets of experiments. By not using absolute values and by only using relative values of strength (relative to a constant such as Young's modulus) obtained from MD data constitutive relations for describing nanocomposite material behavior can be developed. The presented analyses only focus on predicting trends with respect to ideal material strength values due to the presence of features such as interfaces, GBs, and triple junctions. Predictions made can only be made using the MD technique used in the present work. Significant improvements are possible with availability of verifying small scale experiments.

Fig. 1(a) shows the set of Si–C–N microstructures analyzed. Microstructure S1 is a block of Si_3N_4 with 4 nm cylindrical SiC particles uniformly dispersed in the middle. Microstructures S2 and S3 have 4 nm cylindrical SiC particles uniformly dispersed in the middle of two different types of bi-crystalline Si_3N_4 blocks. Microstructures S4 and S5 have a 4 nm cylindrical SiC block placed at the triple junction GB identified in the figure. The cylindrical SiC particles in all atomistic morphologies have their (0 0 1) surface perpendicular to the plane of the figures. Crystalline orientations of Si_3N_4 in all structures are also shown in Fig. 1(a). The microstructures shown in Fig. 1(b) are the same as shown in Fig. 1(a) with one difference at the Si_3N_4 GBs and SiC–Si_3N_4 interfaces. At the Si_3N_4 GBs a 1 nm thick layer of N atoms and at SiC–Si_3N_4 interfaces 5 Å thick layers of C and N atoms, respectively, are placed. The structures in Fig. 1(a) are referred to have *sharp* GBs and interfaces. The structures in Fig. 1(b) are referred to have *diffused* GBs and interfaces. A subscript of 2 is used to differentiate structures in Fig. 1(b) from those shown in Fig. 1(a). As pointed out earlier in Section 1, non-stoichiometric diffused GB and interface structures in Fig. 1(b) are analyzed to understand the effect of the grain boundaries with finite thickness on the overall mechanical strength of the structures. In experiments such diffused structure of GBs has been observed earlier.[16]

Fig. 2 shows the SiCO microstructures analyzed. As discussed earlier the SiCO microstructures are generated based on the two different types of possible morphologies shown in literature.[7–10] In the case of the first type of morphology (type-I), three different nanodomain sizes (9 nm, 6 nm and 4 nm) with two different domain wall thicknesses (0.5 nm $S6_1$, $S7_1$, $S8_1$ and 1 nm $S6_2$, $S7_2$, $S8_2$) consisting of graphitic carbon are considered. In the case of the second type of morphology (type-II), three different samples with three different mean domain sizes (9 nm, 6 nm and 4 nm) are considered. Orientation of grains in nanodomains is chosen randomly. As pointed out earlier, geometrically defined structures shown in Figs. 1 and 2 are equilibrated using canonical ensemble (NVT) equations of motion based on Nose–Hoover thermostat at three different temperatures: 300 K, 900 K, and 1500 K for 100 ps separately. In the end we have 48 different structures with 16 structures obtained after equilibration at each of the three temperatures. Equilibration was performed such that both the total potential and total kinetic energy of a structure stops fluctuating as a function of equilibration time. An additional imposed requirement was that the structures become relaxed with smallest possible change in the structural order as a function of an increase in the equilibration period.

3.1. Analyses of SiC–Si_3N_4 nanocomposites

Fig. 3 shows Si–Si and C–C normalized RDFs for S4 and $S4_2$ microstructures after the MD equilibration. Other structures shown in Fig. 1 (a) and (b) also showed similar attributes as shown by S4 and $S4_2$, respectively. For both structures, normalized RDFs for Si–N and Si–C bonds showed similar characteristics as shown for Si–Si bond. Normalized RDFs for N–N and C–N bonds showed similar characteristics as C–C bond. As shown, there are insignificant changes in all RDFs after equilibration at all temperatures in comparison with the initial un-equilibrated microstructure RDF for S4. In the case of $S4_2$ microstructure, Si–Si (and Si–N as well as Si–C) RDFs remain unchanged after equilibration at all temperatures. However, C–C (and N–N as well as C–N) RDFs change significantly as a function of temperature. The pattern of change includes a shift in

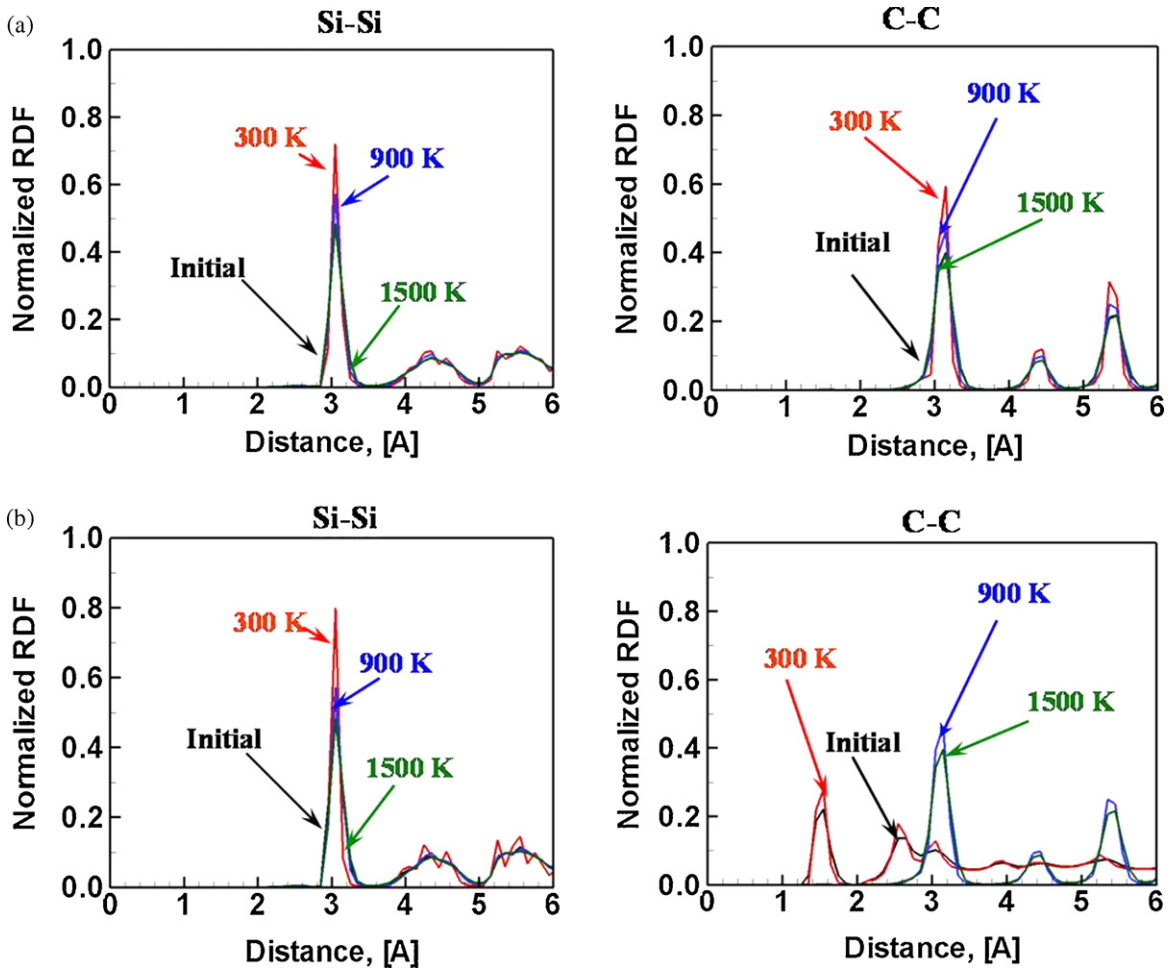

Fig. 3. A comparison of Si–Si and C–C normalized radial distribution functions (RDFs) before equilibration with those after equilibration at 300 K, 900 K, and 1500 K for microstructures (a) S4 and (b) $S4_2$.

peak as well change in full width at half maximum (fwhm). Rightward shift of the peaks indicates bond length relaxation due to overall structural stress gradients that may lead to softening of the diffused GBs and interfaces. A comparison of the curves shown in Fig. 3(a) and (b) reveals that the SiC and Si_3N_4 bulk phases remain relatively unchanged with change in equilibration temperatures. However, in the case of $S4_2$ at the Si_3N_4 GBs and SiC–Si_3N_4 interfaces a significant restructuring of non-stoichiometric C–N phases takes place leading to the changes shown in the C–C, N–N, and C–N RDFs. This indicates that *sharp* GBs and interfaces maintain their structural order and possibly strength at all temperatures. Based on these results it can be concluded that the structures with *sharp* GBs and interfaces show insignificant change in structural order as a function of temperature. On the contrary, the structures with *diffused* GBs and interfaces show significant structural relaxation that may contribute to reduction in peak structural strength leading to softening which may also contribute to increased material resistance against fracture.

Fig. 4 shows stress–strain plots for all the microstructures shown in Fig. 1 at 300 K and 1500 K. The trends at 900 K were in between those shown at 300 K and 1500 K. Microstructure S1 is found to be the strongest microstructure at all temperatures. The major difference between microstructures S1 and S2 is the presence of GBs. The GBs facilitate grain sliding based deformation mechanism leading to the lowering of peak strength. In the case of microstructure S1 the absence of GBs leads to the absence of GB sliding based deformation mechanism, thereby making it stronger. Structures S2 and S3 have the same GB volume fraction and show almost similar peak strength indicating that the orientation of the Si_3N_4 grains at GBs may not be an important factor guiding the peak strength. The same is observed for microstructures S4 and S5. The major difference between microstructures S1 and S4/S5 is the presence of GBs as well as the placement and volume fraction of SiC particles. Structures S4 and S5 have largest volume fraction of GBs leading to the least strength of the microstructures S1 to S5. Overall, it is the volume fraction of atoms in GBs that determines the peak strength with peak strength reducing with increase in the atomic volume fraction in GBs. It should be noted that sample sizes are very small resulting in very high GB volume fraction. The presence of diffused GBs leads to lowering of microstructural strength. However, the presence of diffused GBs does not alter the conclusions reached regarding the deformation mechanism. The extent of the reduction in strength with an increase in the number of GBs and interfaces increases with the presence

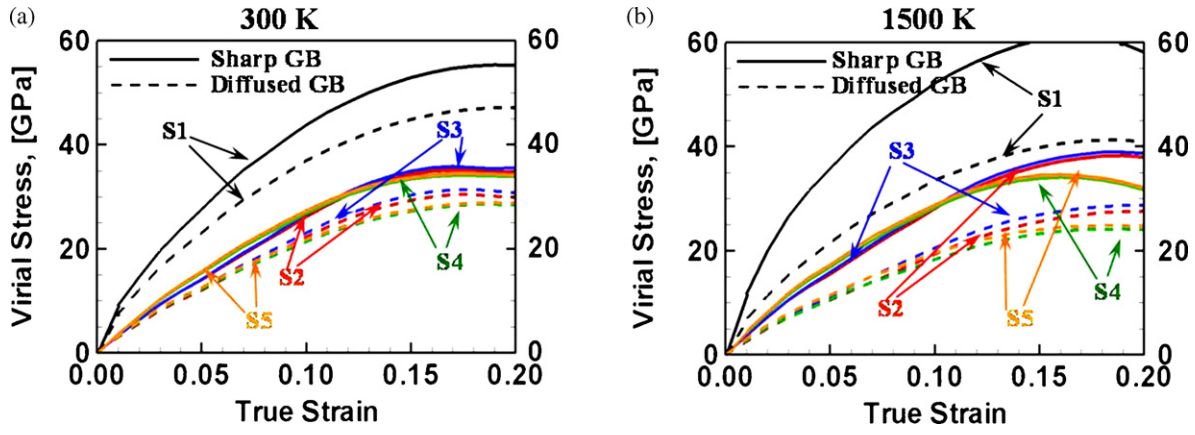

Fig. 4. A comparison of virial stress in loading direction as a function of true strain at (a) 300 K and (b) 1500 K for microstructures shown in Fig. 1.

of diffused GBs and interfaces. A comparison of Fig. 4(a) and (b) reveals that the strength of microstructure S1 increases by approximately 5% with increase in temperature. The increase is about 2–3% for microstructures S2 and S3. The strength of microstructures S4 and S5 reduces with increase in temperature. The strength of diffused GB microstructures $S1_2$ to $S5_2$ reduces uniformly with increase in temperature. The extent of decrease is of the order of 10–30%. The difference between the sharp GB and diffused GB structures widens with increase in temperature.

As pointed out earlier during discussions on Fig. 3 results, structures with diffused GBs have relaxed Si–C, C–N, and Si–N bond lengths that may contribute to their lower strength as well as to the reduction in peak strength with increasing temperatures. Another important factor is the volume fraction of atoms in GBs. Strength of microstructure S1 with no atoms in GBs increases with increase in temperature to 1500 K. The increase is very slight for microstructures S2 and S3, where GBs are now present. In the case of microstructures S4 and S5, there is no increase in strength with temperature increase. A conclusion that can be drawn based on these results is that GBs tend to soften the structure with increase in temperature. Structures with interfaces and no GBs on the other hand become stronger. An increase in the strength for microstructures S1 to S3 with increase in temperature can be explained by considering deformation mechanisms. Second phase SiC particles usually act as stress concentration points in a microstructure. SiC, Si_3N_4 and SiC–Si_3N_4 interfaces soften with increase in temperature. Correspondingly, the extent of stress concentration caused by SiC particles reduces with increase in temperature. This leads to strengthening of structures at higher temperatures. The effect of stress concentration reduction is countered by increased GB sliding with increasing temperature. In microstructures S2 and S3, the effect of stress concentration reduction still dominates. However, in the case of microstructures S4 and S5, the increased GB sliding with increasing temperature dominates leading to reduction of strength. One important result is strength reduction in the case of microstructures $S4_2$ and $S5_2$ with increase in temperature. The difference in material strength between microstructures S4 and $S4_2$ (and S5 and $S5_2$) reduces with increase in temperature. However, due to the presence of diffused GBs, microstructures $S4_2$ and $S5_2$ have much higher strength against fracture than microstructure S4 and S5, respectively. Combining temperature dependent strength and fracture resistance observations, in this case, segregation of C and N atomic impurities at GBs leads to materials with good high temperature strength and fracture resistance.

Fig. 5 shows Si–Si and Si–C RDFs for the S1 and S4 microstructures after stretching to 20% strain at 300 K, 900 K, and 1500 K and compares those with the RDFs for the structures just before equilibration. Normalized RDFs for C–C bonds were similar as those for Si–C bonds for the respective microstructures. RDFs for C–N, N–N, and Si–N bonds showed insignificant change with change in microstructure. From the RDF plots it is also clear that the bond length shift with increase in temperature in the case of Si–C RDFs is higher for the S4 microstructure when compared to those for the S1 microstructure. This indicates that increased GB sliding may be contributing to the strength of S4 being less than that of S1 as well as to the strength reduction of S4 with increase in temperature.

These observations are supported by the plot of deformation viewgraphs for microstructures S1 and S4 at 300 K and 1500 K shown in Fig. 6. Fig. 6 plots the viewgraphs just after failure at 300 K and at 1500 K for both microstructures. As shown in Fig. 6(a) multiple stress concentration sites due to stress concentration caused by SiC particles lead to significant fragmentation. However, the fragmentation is significantly reduced with increase in temperature and the corresponding softening of stress concentration. Failure mechanism in the case of microstructure S4 remains unaffected with temperature increase with GB sliding being the primary contributor. In all cases, the second phase particles act as nucleation site of damage.

In order to understand the role of diffused GBs in the deformation mechanism, the deformation viewgraphs for microstructures $S1_2$ and $S4_2$ at 300 K are shown in Fig. 7. As shown, amorphous C and N impurities in diffused GBs are the points of nucleation of damage. The stress concentration caused by SiC particles nucleates damage at diffused GB-Si_3N_4 interfaces which quickly spreads to Si_3N_4 phase in microstructure S1 and to the adjacent GBs in the microstructure S4. Increase in the amorphous structural order due to diffused GBs leads to increased GB sliding assisted deformation mechanism facilitating the lowering of the microstructural strength.

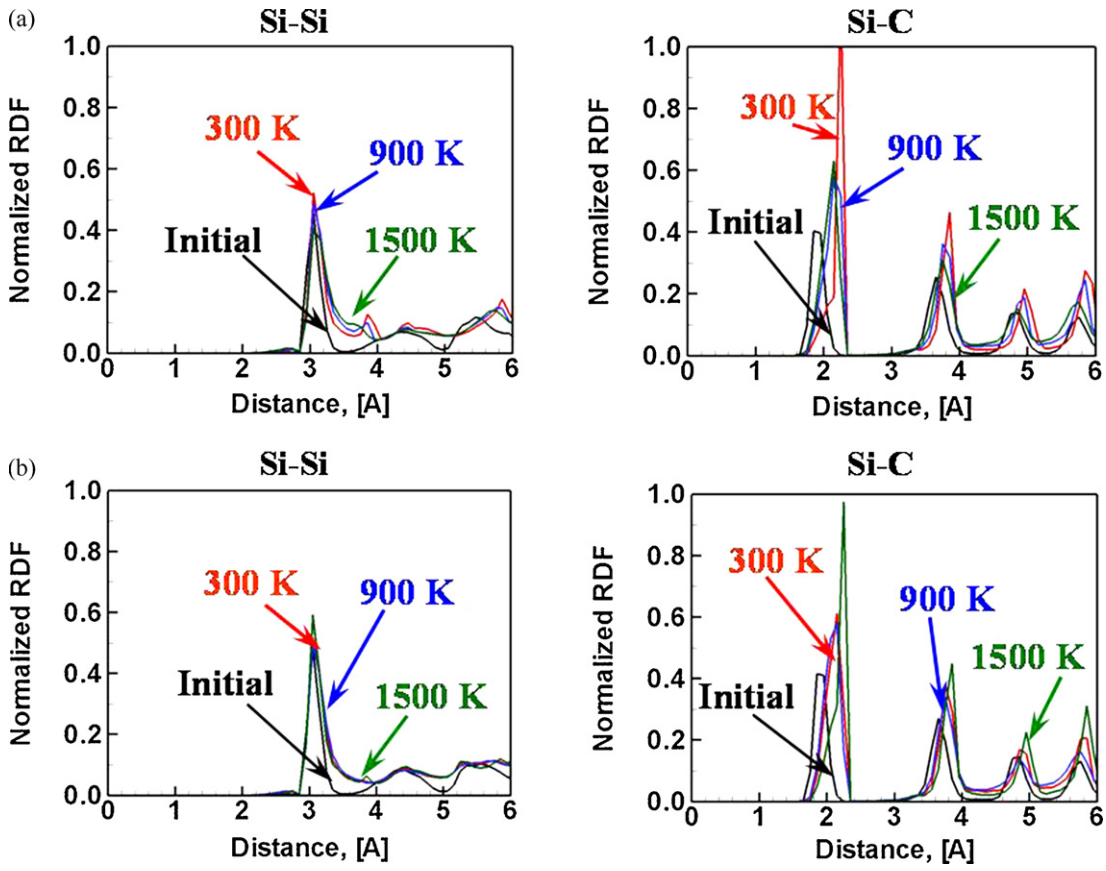

Fig. 5. A comparison of normalized Si–S and Si–C RDFs before stretching with those after stretching at 20% strain at 300 K, 900 K, and 1500 K for microstructures (a) S1 and (b) S4. Normalized RDFs for C–C bonds were similar as those for Si–C bonds for the respective microstructures. RDFs for C–N, N–N, and Si–N bonds showed insignificant change with change in microstructure.

Overall, distribution of SiC particles, volume fraction of atoms in GBs, and GB thickness play an important role in temperature dependent mechanical behavior of SiC–Si_3N_4 nanocomposites. The deformation mechanism is a trade-off between the stress concentration caused by SiC particles and Si_3N_4–Si_3N_4 GB sliding. The temperature increase tends to work in favor of GB sliding leading to softening of structures. However, microstructural strength increases with increase in temperature when GBs are absent.

3.2. Analyses of SiCO nanocomposites

Fig. 8 shows Si–Si and C–C RDFs for microstructures $S6_1$ and S9 after equilibration at 300 K, 900 K, and 1500 K temperatures and compares those with the corresponding RDFs before equilibration. The O–O RDFs before and after equilibration at all temperatures were the same for both microstructures. The RDFs for microstructures $S6_2$, $S7_1$, $S7_2$, $S8_1$, and $S8_2$ showed similar attributes as shown for the microstructure $S6_1$ and, therefore, are not shown. The RDFs for S10 and S11 microstructures showed similar attributes as shown for the microstructure S9 and, therefore, are not shown. It is clear from the Fig. 8(a) that the microstructure $S6_1$ goes through a significant amorphization during equilibration. The crystalline RDF peaks before equilibration turn flat indicating amorphous structure formation after equilibration. The extent of amorphization shows an insignificant dependence on the equilibration temperature. In the case of microstructure S9 (Fig. 8(b)) a partial amorphization of the microstructure takes place. As shown, peaks are still present in the Si–Si and C–C RDFs. However, O–O RDFs after equilibration indicated complete amorphization. A reason for such changes can be that SiO_2 phase becomes amorphous while the SiC phase remains crystalline after equilibration. It is important to note here that equilibration indicates the natural evolution of the microstructure as a function of temperature. While the type-I SiCO microstructure is completely amorphous the type-II SiCO microstructure is partially crystalline. As shown later, such a microstructural difference leads to a significant difference in the material behavior as a function of temperature and other phase defining factors.

Fig. 9 shows the stress–strain behavior of the microstructures $S6_1$, $S6_2$, $S8_1$, and $S8_2$ at 300 K and 1500 K. The trends at 900 K were in between those shown at 300 K and 1500 K. Temperature change has an insignificant effect on the mechanical strength with average strength increasing by almost 1–3% with increment in temperature. It can be concluded that the microstructural strength is insensitive to temperature variation. The change in thickness of nanodomain walls from 0.5 nm to 1 nm leads to reduction in the microstructural strength by approximately 5%. The extent of reduction in strength with increase in domain wall thickness increases with temperature increase.

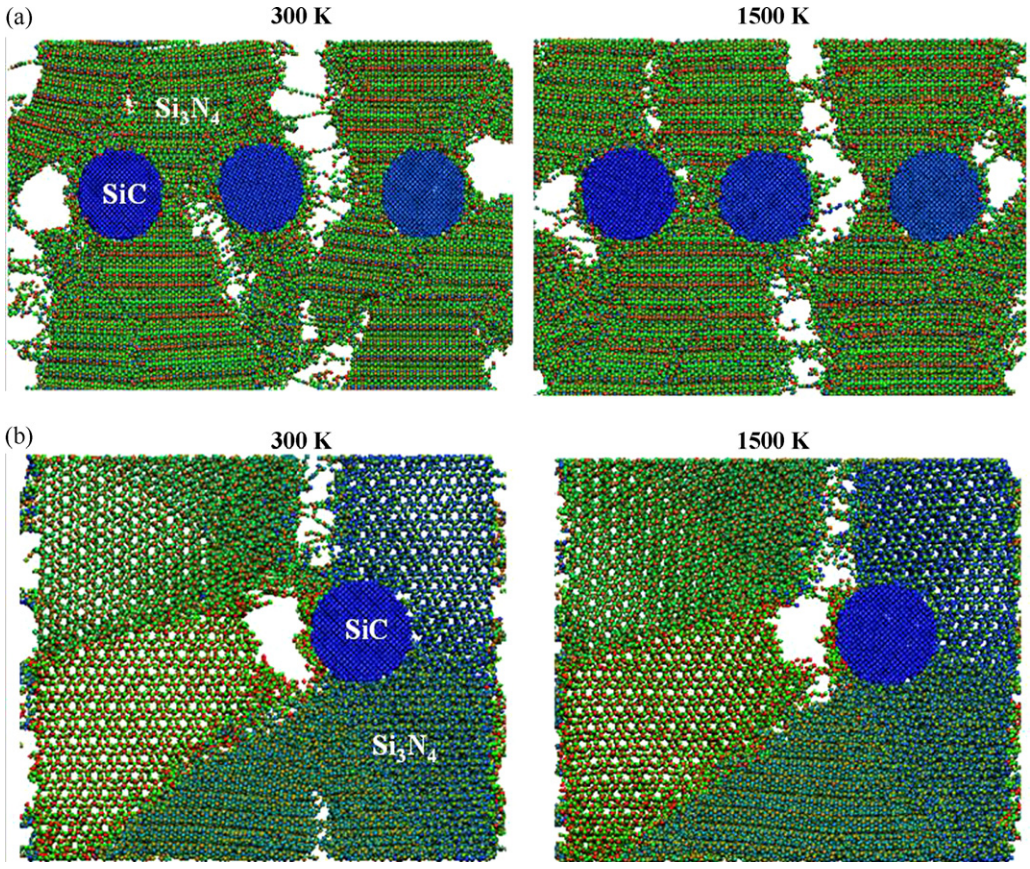

Fig. 6. A comparison of deformation mechanism in microstructures (a) S1 and (b) S4 at 300 K and 1500 K.

The morphology related factors responsible for S6, S7, and S8 microstructures showing softening as a function of reduction in nanodomains size and as a function of increase in nanodomain wall thickness can be understood by analyzing the Si–Si, C–C, and O–O RDFs. Fig. 10 displays Si–Si RDFs for microstructures $S6_1$ (Fig. 10(a)), $S6_2$ (Fig. 10(b)), and $S8_1$ (Fig. 10(c)) after stretching to 20% strain at 300 K, 900 K and 1500 K temperatures and compares these with the corresponding RDFs before equilibration. Similar trends were observed for C–C and O–O RDFs. A comparison of RDFs in Fig. 10(a) and (b) reveals that with increase in nanodomain wall thickness, the Si–Si RDFs are not significantly affected. However, the extent of crystallinity in the nanodomain walls (indicated by the height of C–C peaks) reduces to a significant extent (not shown here). It indicates that with increase in the nanodomain wall thickness and the resulting increase in the amorphization the extent of sliding between the nanodomains increases leading to the softening of microstructures. A comparison of Fig. 10(a) and (c), however, showed that the softening due to reduction in grain size is a result of increased amorphization of the SiO_2 nanodomains (crystalline peaks of Si–Si and O–O RDFs (not shown) were higher indicating higher crystallinity). While softening of microstructures as a function of grain size and as a function of nanodomain wall thickness could be explained using the RDFs, the temperature dependent hardening cannot be explained. Since the extent of temperature dependent hardening is not significant, the

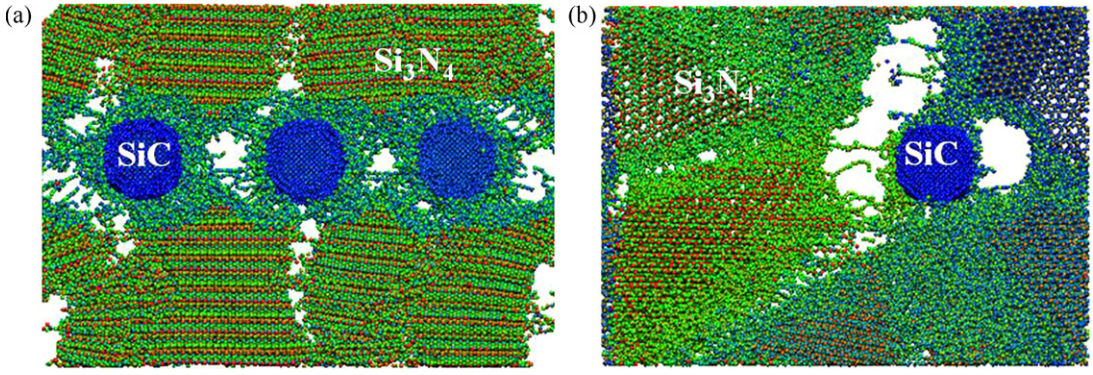

Fig. 7. A comparison of deformation mechanism in microstructures (a) $S1_2$ and (b) $S4_2$ at 300 K.

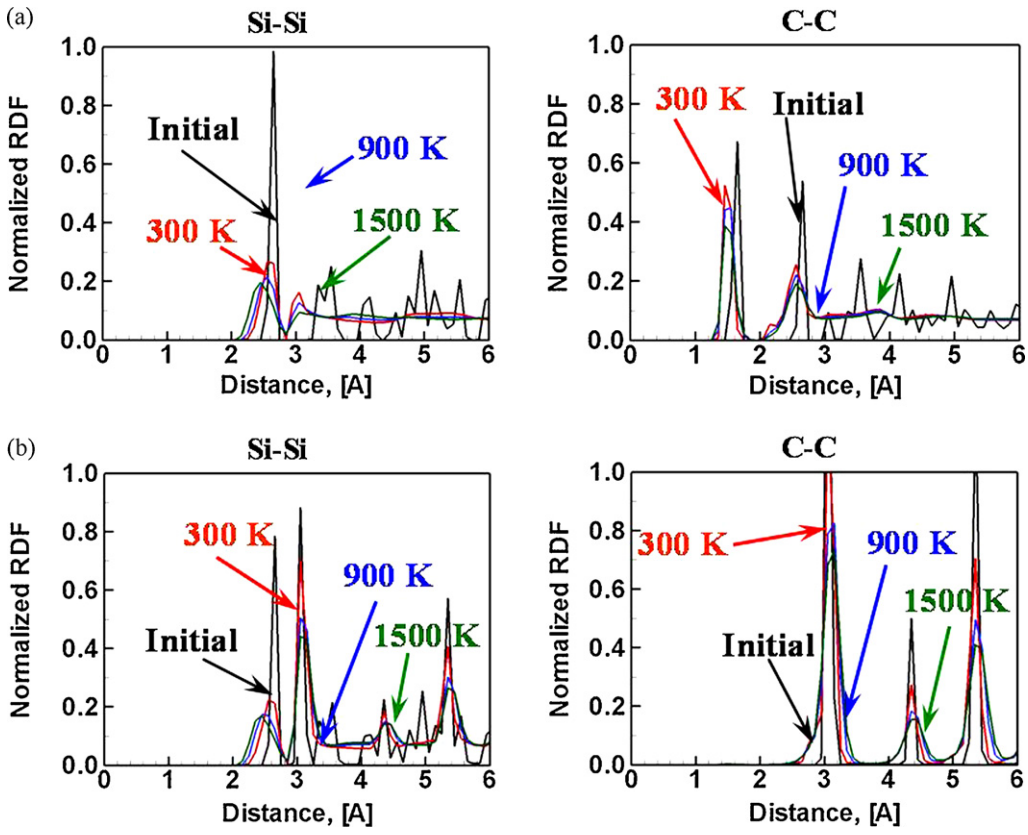

Fig. 8. A comparison of Si–Si and C–C normalized RDFs before equilibration with those after equilibration at 300 K, 900 K, and 1500 K for microstructure (a) $S6_1$ and for microstructure (b) S9. O–O RDFs before and after equilibration at all temperatures were the same for both microstructures.

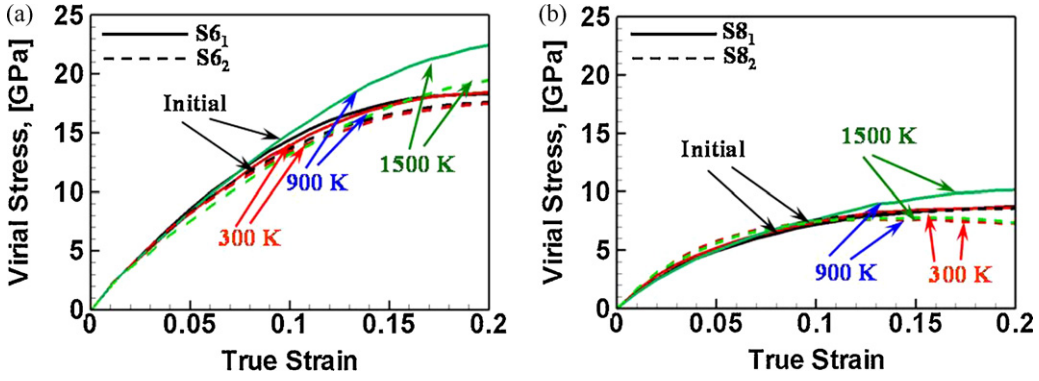

Fig. 9. A comparison of virial stress in loading direction as a function of true strain at all temperatures for microstructures (a) $S6_1$ and $S6_2$ and for microstructures (b) $S8_1$ and $S8_2$.

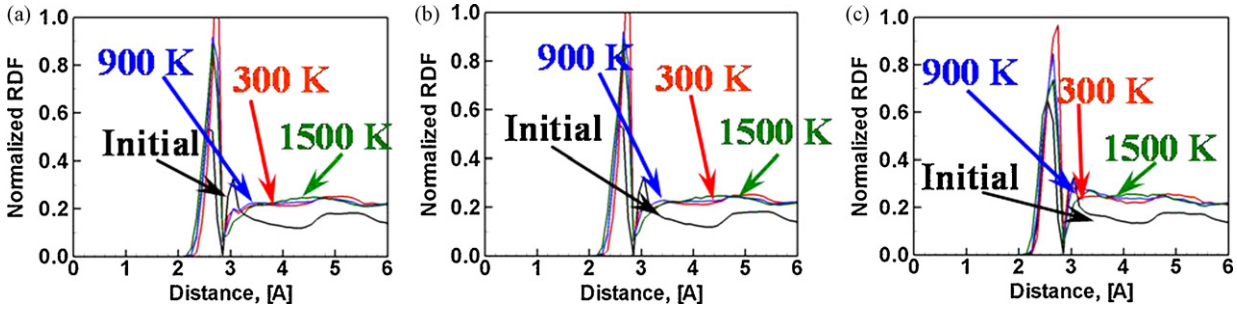

Fig. 10. A comparison of normalized Si–Si normalized RDFs before stretching with those after stretching at 20% strain at 300 K, 900 K, and 1500 K for microstructures (a) $S6_1$, (b) $S6_2$ and (b) $S8_1$. As shown insignificant difference as a function of temperature in the RDFs after stretching was observed. Similar trends were observed for C–C and O–O RDFs.

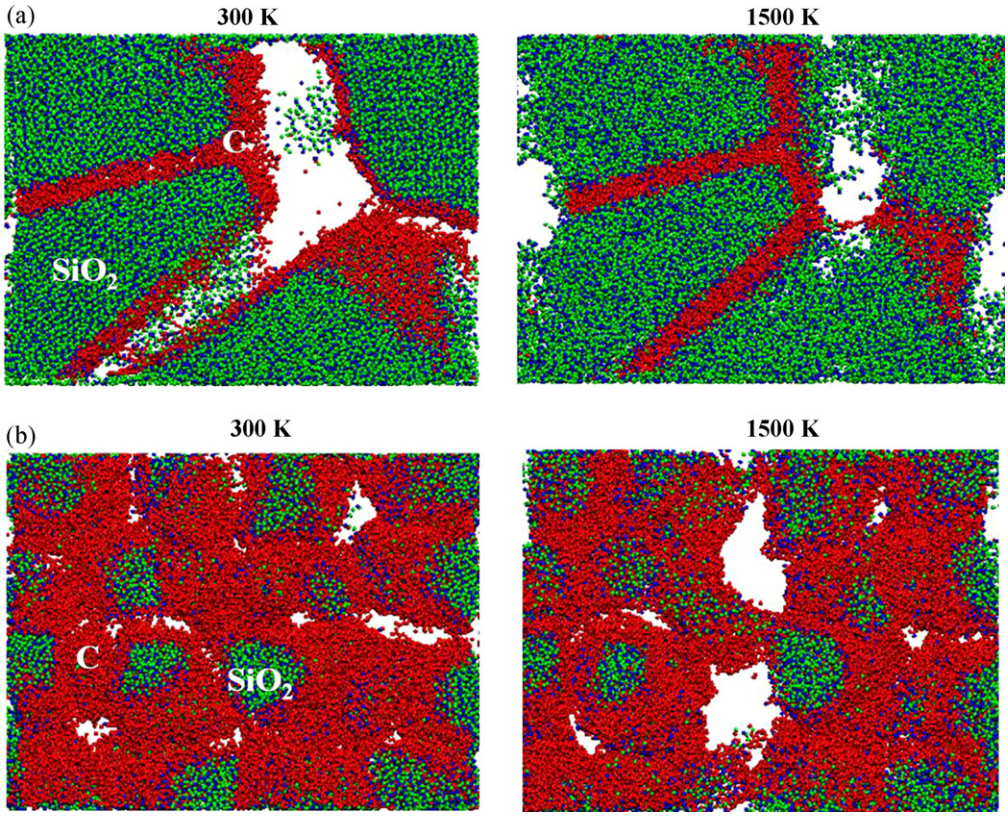

Fig. 11. A comparison of deformation mechanism in microstructures (a) $S6_1$ and (b) $S8_1$ at 300 K and 1500 K.

related changes in RDFs as a function of temperature increase are insignificant.

In order to understand the role of wall thickness, nanodomain size, and temperature in mechanical deformation, the deformation viewgraphs of the structures discussed in Fig. 10 are shown in Fig. 11. As shown in Fig. 11(a), increase in temperature leads to fracture being along GBs as well as inside grain interiors. At 300 K, the fracture is solely due to nanodomain boundary sliding and separation. At 1500 K, however, carbon based nanodomain boundaries are strengthened. The fracture initiates in SiO_2 interiors softened by temperature. A combined effect is increase in strength with increase in temperature. As shown in Fig. 11(b) the same reasoning can be applied to microstructure $S8_1$ as well. A comparison of plots shown in Fig. 10 earlier shows that temperature increase dependent strengthening is higher for $S6_1$ than $S8_1$. This is also confirmed in Fig. 11. The structure S81 has unusually high fraction of C atoms. Therefore, domain boundary strengthening cannot negate the sliding based deformation mechanism. This directly leads to lesser increase in strength in comparison to microstructure $S6_1$. The softening related to grain size reduction can be explained from the observation of damage in Fig. 11, where a significant damage in both $S6_1$ and $S8_1$ microstructure nanodomain walls can be seen as a function of applied deformation. The damage in the nanodomain walls reduces with increase in temperature. However, this leads to greater facilitation of interdomain sliding based deformation mechanism leading to the softening of these structures with reduction in grain size.

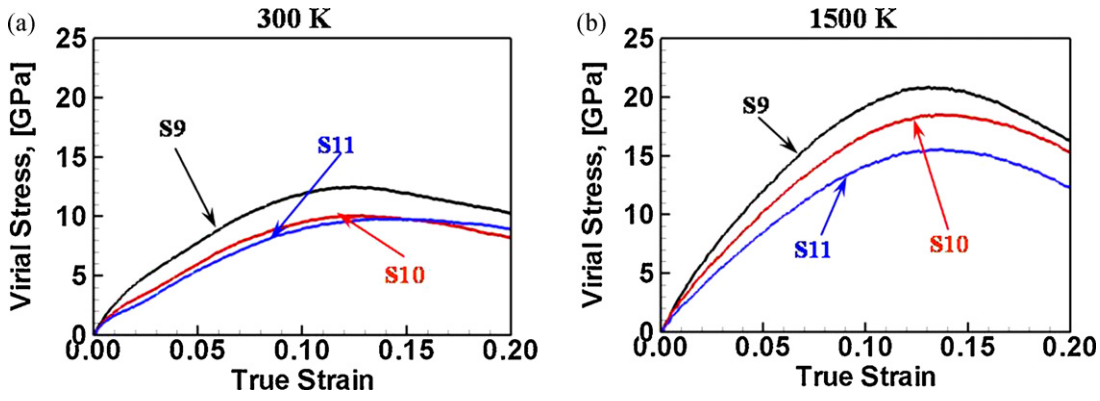

Fig. 12. A comparison of virial stress in loading direction as a function of true strain for microstructures S9, S10, and S11 at (a) 300 K and at (b) 1500 K.

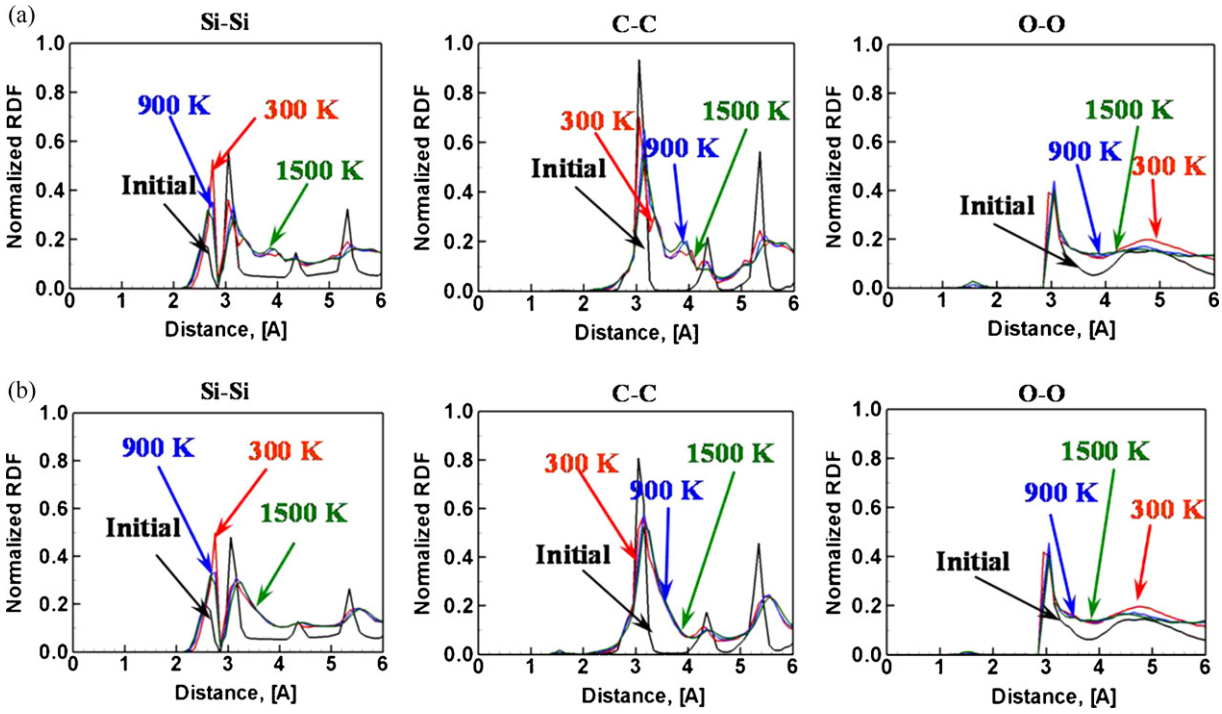

Fig. 13. A comparison of normalized Si–Si, C–C and O–O radial distribution functions (RDFs) before stretching with those after stretching at 20% strain at 300 K, 900 K, and 1500 K for microstructures (a) S9 and (b) S11.

Fig. 12 shows stress–strain plots for microstructures S9, S10, and S11 at 300 K and 1500 K. As shown, all microstructures show hardening with increase in temperature and softening with reduction in domain size. The softening with reduction in nanodomain size and hardening with increase in temperature are in accordance with the behavior observed for type-I microstructures earlier. The mechanism is also the same. However, in this case the magnitude of hardening is much higher. The factor that could be attributed to causing such an effect is the presence of SiC domains instead of C based domain boundaries.

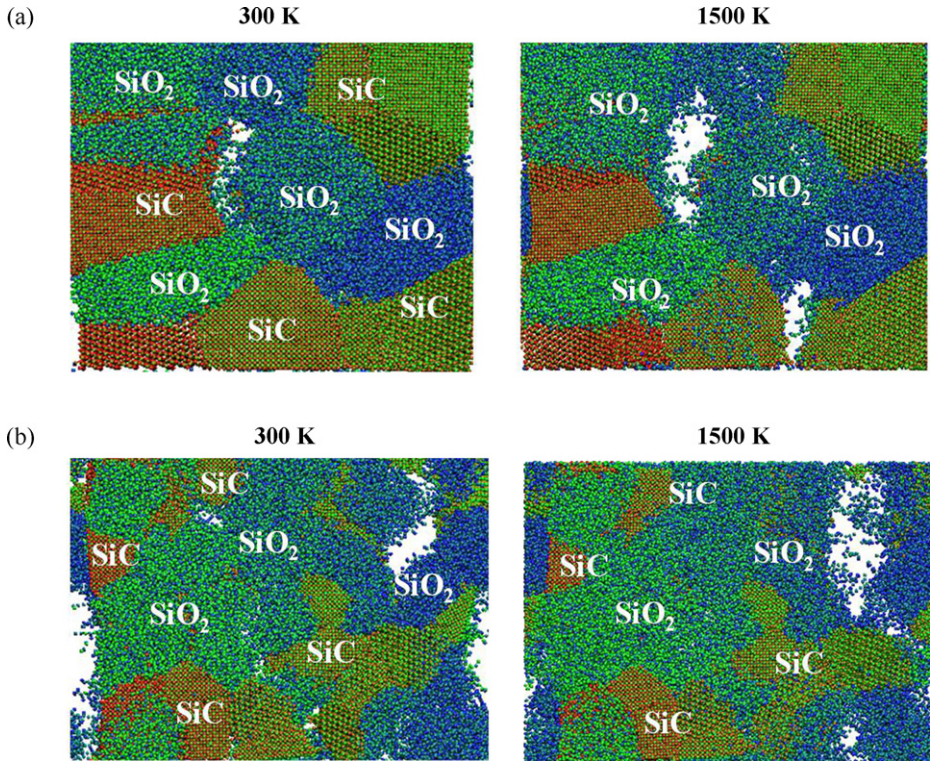

Fig. 14. A comparison of deformation mechanism in microstructures (a) S9 and (b) S11 at 300 K and 1500 K.

Fig. 13 shows Si–Si, C–C, and O–O RDFs for microstructures S9 (Fig. 12(a)) and S11 (Fig. 12(b)) after stretching to 20% strain at 300 K, 900 K and 1500 K temperatures and compares these with the corresponding RDFs before equilibration. The O–O RDFs for both microstructures S9 and S11 show similar attributes. However, the Si–Si and C–C RDFs are different in the extent of amorphization. As shown the amorphization extent increases with reduction in nanodomain size. The Si–Si and C–C RDFs for microstructure S9 show sharp peaks remaining after equilibration. However such peaks disappear for the S11 microstructure with smaller nanodomain size. The strength hardening with increase in temperature cannot be explained from RDFs since the temperature related changes in the RDFs are insignificant. In order to understand the deformation mechanism as a function of grain size and as a function of temperature, the deformation viewgraphs for the S9 and S11 microstructures are compared in Fig. 14. The nanodomain wall like structures important for S6, S7, and S8 microstructures are absent in S9, S10, and S11 microstructures. Since the SiO_2 nanodomains are amorphous, the extent of interdomain sliding is limited only to the crystalline SiC nanodomains with the sliding increasing with increase in SiC amorphization. With reduction in grain size the extent of SiC amorphization increases facilitating the interdomain sliding based deformation mechanism. This directly leads to softening of the microstructures with reduction in grain size. At all grain sizes failure invariably initiated in SiO_2 grains. With increase in temperature the extent of interdomain sliding reduces for all microstructures. This is clear from Fig. 14 snapshots at 1500 K where the fracture initiates in higher number of locations. Owing to limited sliding, stress concentration due to deformation is effective in fracture initiation in higher number of locations in the microstructures. At the same time, reduced sliding makes the structures stronger against applied deformation.

Overall, temperature change, the nanodomain wall placement, the nanodomain wall thickness, and nanodomain size are important factors that directly affect the extent of crystallinity and the corresponding strength against mechanical deformation in both types of the SiCO microstructures. Type-II showed higher sensitivity to domain size change and to temperature increase. The extent of crystallinity is directly correlated to interdomain sliding based deformation mechanism that ultimately determines the microstructural strength of the SiCO systems examined.

4. Conclusions

In the present work MD based analyses to understand the effect of morphology on the mechanical behavior of two important high temperature material systems at three different temperatures (300 K, 900 K, and 1500 K) are presented. The analyses focused on understanding the effect of three different structural aspects in the case of SiCN material system: (1) Si_3N_4 crystalline orientation, (2) GB and interface volume fraction (number of GBs and interfaces) and (3) particle arrangement with respect to the GBs. In the case of SiCO system, analyses focused on understanding the effect of (1) type of material system, (2) nanodomain size and (3) nanodomain wall thickness. The morphology related factors were found to be strongly coupled with the temperature of study. Results were analyzed using a combination of mechanical stress–strain curves, RDF plots, and visual observations of mechanical deformation. The crack path resistance and fracture resistance could not be analyzed because of the existence of fault tolerance at the length scale of study.[14] However, simple mechanical strength analyses offered good insights into the phase morphology effect on temperature dependent microstructural strength.

In the case of SiCN system analyses indicated that the second phase particles act as significant stress raisers in the case of single crystalline Si_3N_4 phase matrix reducing the nanocomposite mechanical strength. Deformation mechanism consists of considerable ductile tearing at the SiC–Si_3N_4 interfaces in all structures. Strength reduced with increase in the GB and interface atom volume fraction at all temperatures. Strength for some structures with sharp GBs and interfaces increased with increase in temperature (S1, S2, and S3). However, structures deforming under strong influence of GB sliding showed decrease in strength in increase in temperature (S4 and S5). The strength of structures with diffused GBs decreased with increase in temperature. Without exception, microstructures with diffused GBs were found to be softer than the microstructures with sharp GBs. The finding indicated that distribution of SiC particles, volume fraction of atoms in GBs, and GB thickness play an important role in temperature dependent mechanical behavior of SiC–Si_3N_4 nanocomposites. The deformation mechanism is a trade-off between the stress concentration caused by SiC particles and Si_3N_4–Si_3N_4 GB sliding. The temperature increase tends to work in favor of GB sliding leading to softening of structures. However, microstructural strength increases with increase in temperature when GBs are absent.

In the case of SiCO system, the extent of amorphization dictated the primary deformation mechanism of inter nanodomain sliding for type-I microstructures. In the absence of nanodomain boundaries type-II microstructure deformation was strongly influenced by extent of crystallinity. Of the two types of classifications studied for this material system, the type-I system with nanodomain walls of C atoms showed strengthening with increase in temperature, softening with reduction in domain size, and softening with increase in the nanodomain wall thickness. Primarily the amorphization of the nanodomain walls facilitated interdomain sliding. Factors that led to smaller nanodomain wall thickness resulted in stronger microstructure and vice versa. Type-II system without nanodomain walls but with SiC and SiO_2 particles mixed in the form of nanodomains to form a composite structure showed softening with reduction in grain size and hardening with increase in temperature. Type-II showed higher sensitivity to domain size change and to temperature increase in comparison to type-I. In all cases the SiO_2 nanodomains were amorphous. The extent of amorphization of SiC nanodomains was driven by temperature and grain size with higher amorphization leading to weaker microstructure. Overall, temperature change, the nanodomain wall placement, the nanodomain wall thickness, and nanodomain size are important factors that directly affect the extent of crystallinity and the

corresponding strength against mechanical deformation in both types of the SiCO microstructures.

Overall, analyses confirm that the temperature dependent strengthening or softening in both the nanocomposite material systems is a function of GB/nanodomain wall thickness, particle placement, grain/nanodomain size, and temperature. It is important to note here that stress–strain based results from MD are at very high strain rates on very pure idealized samples. Due to high rates and high purity, strength value predictions are very high in MD simulations. In the absence of experiments at such high strain rates as used in MD, it is not possible to verify or deny MD simulation results. In the absence of experimental validations, MD simulation results can be used to predict trends on the effect of morphology on strength. The presented analyses only focus on predicting trends with respect to ideal material strength values due to the presence of features such as interfaces, GBs, and triple junctions, etc. Predictions made can only be made using the MD technique used in the present work. Significant improvements are possible with availability of verifying small scale experiments.

At the simulation length scale we observed flaw-tolerance.[14] Therefore, we cannot model the crack path resistance. However, by increasing the length scale of the simulations crack path resistance analyses are possible. One way to use the presented simulations is modeling higher length scale crack path resistance behavior in a multiscale framework. The trends and maximum strength values could be supplied in higher length scale models such as the cohesive finite element method (e.g. Refs. 11,12) that could predict the crack path resistance while considering the nanoscale morphology effects. Similarly, temperature dependent material models from the reported simulations could be used to study creep behavior of the materials at higher length and timescales. These investigations are subjects of ongoing work.

Acknowledgement

The authors acknowledge support from the Air Force Office of Scientific Research-AFoSR (Program Manager: Dr. Joan Fuller).

References

1. Weimer AW, Bordia RK. Processing and properties of nanophase SiC/Si_3N_4 composites. *Compos Part B: Eng* 1999;**30**:647–55.
2. Ajayan PM, Schadler LS, Braun PV. *Nanocomposite science and technology*. Wiley-VCH; 2003.
3. Niihara K. New design concept for structural ceramics-ceramic nanocomposites. *J Ceram Soc Jpn: The Centennial Memorial Issue* 1991;**99**(10):974–82.
4. Ohji T, Jeong Y-K, Choa Y-H, Niihara K. Strengthening and toughening mechanisms of ceramic nanocomposites. *J Am Ceram Soc* 1998;**81**(6):1453–60.
5. Rendtel A, Hubner H, Herrman M, Schubert C. Silicon nitride/silicon carbide nanocomposite materials: II. Hot strength, creep, and oxidation resistance. *J Am Ceram Soc* 1998;**81**(5):1109–20.
6. Bois L, Maquet J, Babonneau F, Bahloul D. Structural characterization of sol–gel derived oxycarbide glass. 2. Study of thermal stability of silicon oxycarbide phase. *Chem Mater* 1995;**7**:975–81.
7. Kleebe H-J, Turquat C, Soraru GD. Phase separation in an SiCO glass studied by transmission electron microscopy and electron energy-loss spectroscopy. *J Am Ceram Soc* 2001;**84**(5):1073–80.
8. Saha A, Raj R, Williamson DL, Kleebe H-J. Characterization of nanodomains in polymer-derived SiCN ceramics employing multiple techniques. *J Am Ceram Soc* 2005;**88**(1):232–4.
9. Saha A, Raj R, Williamson DL. A model for the nanodomains in polymer-derived SiCO. *J Am Ceram Soc* 2006;**89**(7):2188–95.
10. Saha A, Raj R. Crystallization maps for SiCO amorphous ceramics. *J Am Ceram Soc* 2007;**90**(2):578–83.
11. Tomar V. Analyses of the role of the second phase SiC particles in microstructure dependent fracture resistance variation of SiC–Si_3N_4 nanocomposites. *Model Simul Mater Sci Eng* 2008;**16**:035001.
12. Tomar V. Analyses of the role of grain boundaries in mesoscale dynamic fracture resistance of SiC–Si_3N_4 intergranular nanocomposites. *Eng Fract Mech* 2008;**75**:4501–12.
13. Tomar V, Samvedi V. Atomistic simulations based understanding of the mechanism behind the role of second phase SiC particles in fracture resistance of SiC–Si_3N_4 nanocomposites. *Int J Multiscale Comput Eng* 2009; **7**(4): 277–94.
14. Tomar V, Samvedi V, Kim H. Atomistic understanding of the particle clustering and particle size effect on the room temperature strength of SiC–Si_3N_4 nanocomposites. *Int J Multiscale Comput Eng Special Issue on Advances in Computational Materials Science* 2010; **8**(4).
15. Bill J, Kamphowe TW, Mueller A, Wichmann T, Zern A, Jalowieki A, Mayer J, Weinmann M, Schuhmacher J, Mueller K, Peng J, Seifert HJ, Aldinger F. Precursor-derived Si–(B–)C–N ceramics: thermolysis, amorphous state, and crystallization. *Appl Organomet Chem* 2001;**2001**(15):777–93.
16. Jalowiecki A, Bill J, Aldinger F, Mayer J. Interface characterization of nanosized B-doped Si_3N_4/SiC ceramics. *Compos Part A* 1996;**27A**:721.
17. Dionald WARD, Curtin WA, Yue Q. Mechanical behavior of aluminum–silicon nanocomposites: a molecular dynamics study. *Acta Mater* 2006;**54**(17):4441–51.
18. Song M, Chen L. Molecular dynamics simulation of the fracture in polymer-exfoliated layered silicate nanocomposites. *Macromol Theory Simul* 2006;**15**(3):238–45.
19. Tomar V, Zhou M. Analyses of tensile deformation of nanocrystalline α-Fe_2O_3 + fcc-Al composites using classical molecular dynamics. *J Mech Phys Solids* 2007;**55**:1053–85.
20. Zeng QH, Yu AB, Lu GQ. Molecular dynamics simulations of organoclays and polymer nanocomposites. *Int J Nanotechnol* 2008;**5**(2–3):277–90.
21. Zeng QH, Yu AB, Lu GQ, Standish RK. Molecular dynamics simulation of organic–inorganic nanocomposites: layering behavior and interlayer structure of organoclays. *Chem Mater* 2003;**15**:4732–8.
22. Tsuruta K, Totsuji H, Totsuji C. Neck formation processes of nanocrystalline silicon carbide: a tight-binding molecular dynamics study. *Philos Mag Lett* 2001;**81**(5):p357.
23. Tsuruta K, Totsuji H, Totsuji C. Parallel tight-binding molecular dynamics for high-temperature neck formation processes of nanocrystalline silicon carbide. *Mater Trans* 2001;**42**(11):p2261.
24. Mirgorodsky AP, Baraton MI, Quintard P. Lattice dynamics and prediction of pressure-induced incommensurate instability of a β-Si_3N_4 lattice with a simple mechanical model. *Phys Rev B* 1993;**48**(18):13326–32.
25. Lidorikis E, Bachlechner ME, Kalia RK, Nakano A, Vashishta P, Voyiadjis GZ. Coupling length scales for multiscale atomistic-continuum simulations: atomistically induced stress distributions in Si/Si_3N_4 nanopixels. *Phys Rev Lett* 2001;**87**(8):086104.
26. Tomar V, Zhou M. Tension-compression strength asymmetry of nanocrystalline α-Fe_2O_3 + *fcc*-Al ceramic–metal composites. *Appl Phys Lett* 2006;**88**(1–3):p233107.
27. Wendel JA, Goddard WA. The Hessian biased force field for silicon nitride ceramics: predictions of thermodynamic and mechanical properties for α- and β-Si_3N_4. *J Chem Phys* 1992;**97**(7):5048–62.
28. Mota FdB, Justo JF, Fazzio A. Hydrogen role on the properties of amorphous silicon nitride. *J Appl Phys* 1999;**86**(4):1843–7.

29. Kroll PM. Computer simulations and X-ray absorption near edge structure of silicon nitride and silicon carbonitride. PhD thesis, Technische Hochschule Darmstadt, Darmstadt, Germany; 1996.
30. Ching W-Y, Xu Y-N, Gale JD, Ruehle M. Ab-initio total energy calculation of α- and β-silicon nitride and the derivation of effective pair potentials with application to lattice dynamics. *J Am Ceram Soc* 1998;**81**(12):3189–96.
31. Matsunaga K, Iwamoto Y. Molecular dynamics study of atomic structure and diffusion behavior in amorphous silicon nitride containing boron. *J Am Ceram Soc* 2001;**84**(10):2213–9.
32. Rouxel T, Sangleboeuf J-C, Huger M, Gault C, Besson J-L, Testu S. Temperature dependence of Young's modulus in Si_3N_4 based ceramics: roles of sintering additives and of SiC particle content. *Acta Mater* 2002;**50**(7):1669–82.
33. Morkoc H, Strite S, Gao GB, Lin ME, Sverdlov B, Burns M. Large-band-gap SIC, III–V nitride, and II–VI ZnSe-based semiconductor device technologies. *J Appl Phys* 1994;**76**(3):1363–98.
34. Tersoff J. Empirical interatomic potential for silicon with improved elastic properties. *Phys Rev B* 1988;**38**:9902–5.
35. Tersoff J. Modeling solid-state chemistry: interatomic potentials for multicomponent systems. *Phys Rev B (Rapid Commun)* 1989;**39**(8):5566–8.
36. Tersoff J. Carbon defects and defect reactions in silicon. *Phys Rev Lett* 1990;**64**:1757–60.
37. Noreyan A, Amar JG, Marinescu I. Molecular dynamics simulations of nanoindentation of β-SiC with diamond indenter. *Mater Sci Eng B* 2005;**117**:235–40.
38. Umeno Y, Kitamura T, Date K, Hayashi M, Iwasaki T. Optimization of interatomic potential for Si/SiO_2 system based on force matching. *Comput Mater Sci* 2002;**25**:447–56.
39. Matsunaga K, Fisher C, Matsubara H. Tersoff potential parameters for simulating cubic boron carbonitrides. *Jpn J Appl Phys* 2000;**39**:L48–51.
40. Tomar V. *Atomistic modeling of the Al + Fe_2O_3 material system using classical molecular dynamics, in Mechanical Engineering.*. Atlanta: Georgia Institute of Technology; 2005. p. 295.
41. Smith W, Yong CW, Rodger PM. DL_POLY: application to molecular simulation. *Mol Simul* 2002;**28**(5):385–471.
42. Melchionna S, Ciccotti G, Holian BL. Hoover NPT dynamics for systems varying in shape and size. *Mol Phys* 1993;**78**(3):533–44.
43. Zhou M. A new look at the atomic level virial stress—on continuum-molecular system equivalence. *Proc R Soc Lond A* 2003;**459**:2347–92.